Anisotropic Convective Heat Transfer in Microlattice Materials

Christopher S. Roper, Kathryn D. Fink, Samuel T. Lee, Joanna A. Kolodziejska, and Alan J. Jacobsen
HRL Laboratories, LLC, 3011 Malibu Canyon Rd, Malibu, CA 90265

DOI 10.1002/aic.13821
Published online May 1, 2012 in Wiley Online Library (wileyonlinelibrary.com).

Fluid dynamics and heat transfer of flow through periodic open-cellular microlattice structures are characterized for varying superficial flow orientations and flow rates to investigate heat transfer and pressure loss anisotropy. For given Reynolds number, friction factor is lowest when flow is aligned with the largest straight-through passages in the microlattice. A maximum friction factor, over twice the optimally aligned friction factor, exists for flow orientations between $\pi/8$ and $\pi/4$ rad off the optimal alignment, with little variation in friction factor for $\pi/8$ and $\pi/4$ rad. Heat transfer is maximized at $\pi/4$ rad off axis from the largest straight-through passages; however, less angular variation occurs in Nusselt number than in friction factor. Empirical correlations involving superellipses yield analytical equations describing Nusselt number dependence on flow angle and Reynolds number. This work enables selection of optimal flow orientations and optimal cellular architecture in convective heat transfer implementations of microlattice materials for lightweight and multifunctional applications. © 2012 American Institute of Chemical Engineers *AIChE J,* 59: 622–629, 2013
Keywords: fluid mechanics, porous media, heat transfer

Introduction

Extended surface heat transfer structures,[1] including heat sinks and cold plates, are important for electronics,[2] automotive, and aerospace cooling applications. Such structures entail a base surface and an extended surface attached to the base surface. The extended surface can take the form of one or more geometries, including plate fins, pin fins,[3] louvered fins, sintered particles,[4] cellular materials[5–9] including metal foams,[10–16] and truss structures.[17] These geometries enhance heat transfer in two pathways, both through increased mixing providing enhanced convective heat transfer directly to the base surface as well as convection to the extended surface in series with conduction to the base surface.[3] Certain geometries such as fibrous media and porous beds can increase the convective heat transfer directly to the base surface, but their series convection–conduction pathway does not significantly contribute to heat transfer enhancement.[18,19]

Recently, a process has been developed to fabricate ordered open-cellular microlattice materials via a self-propagating photopolymer waveguide process.[20–23] This process is capable of rapidly fabricating ordered open-cellular materials with feature sizes comparable to stochastic microscale foams; however, the ordered open-cellular architecture can be designed to exhibit a lower pressure drop than traditional random open-cellular foams for the same external dimensions.[24,25] The effect of superficial flow direction through these microlattice materials on friction factor has been noted for two flow directions,[25] but it has not yet been systematically investigated. Additionally, the effect of superficial flow direction on the heat transfer characteristics of these materials remains unexplored.

Correspondence concerning this article should be addressed to C. S. Roper at csroper@hrl.com.

In this work, we characterize the fluid dynamics and heat transfer behaviors of fluid flow through microlattice materials as functions of flow rate and for seven superficial flow angles. We then develop angular-dependent correlations to describe the measured fluid flow and heat transfer behavior. Finally, we compare the dimensionless fluid flow and heat transfer results to yield optimal flow orientations for simultaneous high heat transfer and loss pressure drop.

Methods

Open-cellular polymer microlattice samples are fabricated from an interconnected network of self-propagating photopolymer waveguides.[20] Briefly, the process exposes a reservoir of photosensitive monomer precursor through a mask to collimated ultraviolet (UV) light. The mask used to fabricate all samples in this work consists of a square array of circular apertures with diameter (D) of 158 μm and center-to-center spacing (L) of 1.58 mm. Four collimated UV beams generated from a mercury arc lamp, each oriented $2\pi/9$ rad from the mask normal and positioned at $\pi/2$ rad intervals to each other, are used to generate waveguides in the monomer reservoir that initiate at each aperture on the mask in the direction of each incident beam. The waveguides intersect at nodes and continue propagating to form a complete microlattice structure. The resulting microlattice unit cell for this particular fabrication set-up is shown in Figure 1a. It should be noted that this is just one of many possible unit cell architectures.[23] The measured node diameter (D_n) of 326 μm is used as the length scale in the Reynolds and Nusselt numbers. The porosity, or open volume fraction (ε_v), of the resulting microlattice is 0.854. The microlattice samples are postcured for 9×10^4 s at 373 K. Further details regarding the polymer microlattice fabrication process can be found elsewhere.[20]

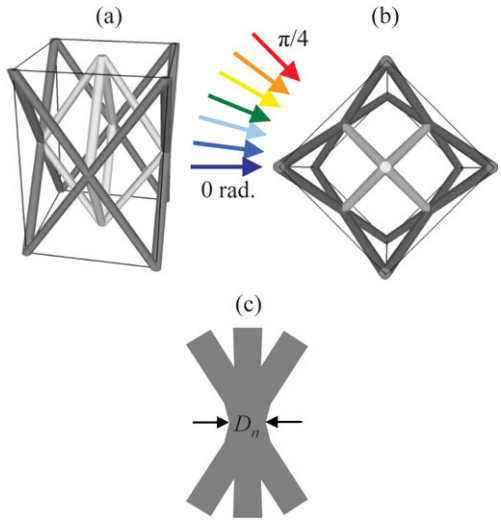

Figure 1. Schematic of octahedral unit cell (a) perspective view, (b) top view with flow orientations, and (c) detail side view of node indicating node diameter, D_n, which is larger than the strut diameter.

[Color figure can be viewed in the online issue, which is available at wileyonlinelibrary.com.]

To measure the fluid flow characteristics of the microlattice structure, 2.6 cm × 10.2 cm × 1 cm thick samples are cut from larger pieces of microlattice material. The longest dimension is oriented at a set angle (φ) from the unit cell basis vector for each sample. Angles of 0, $\pi/24$, $\pi/12$, $\pi/8$, $\pi/6$, $5\pi/24$, and $\pi/4$ rad are selected (Figure 2). Examining 0–$\pi/4$ rad is sufficient to fully characterize the flow in the plane of the sample due to D_{4h} group symmetry[26] of the microlattice unit cell (Figure 1). This unit cell architecture repeats every $\pi/2$ rad and every $\pi/4$ rad section is a mirror image of the adjacent $\pi/4$ rad sections. Each sample is placed in a chamber with interior dimensions matching the exterior dimensions of the sample. Deionized water is passed through the test chamber using a Trident Engineering M1443 pump, while the flow rate is measured by a Cynergy3 ultrasonic flowmeter (Figure 3a). Differential pressure is measured with an Omega PX2300 differential pressure transducer between the inlet and each of five pressure ports beginning 1.3 cm past the inlet and spaced 1.9 cm apart along the centerline of the test chamber. Further details on the fluid flow measurement apparatus can be found elsewhere.[25]

To measure the heat transfer characteristics of the microlattice structure, the same 2.6 cm × 10.2 cm × 1 cm thick samples are placed in a test chamber with interior dimensions matching the exterior dimensions of the sample. A 2.6 cm × 7.6 cm section of one interior wall of the test chamber consists of a heated copper block. The rest of the test chamber is thermally insulated. Each microlattice sample is positioned such that flow develops in the 2.6 cm long unheated region before entering the 7.6 cm long heated region. Deionized water maintained at a constant temperature by a Lydall Affinity F-series Chiller passes through a flow control valve, Cynergy3 ultrasonic flowmeter, and the test chamber before returning to the chiller (Figure 3b). The water temperature is measured at the inlet and outlet of the chamber by two K-type thermocouples, while the surface temperature of the copper wall is measured by six K-type thermocouples embedded in the copper block 2 mm away from the wall and thermally connected to the copper block with Sn–Ag solder.

From the experimental data, the volumetric flow rate ($\dot{V}$), chamber cross-sectional area (A_{flow}), node diameter (D_n), open volume fraction (ε_v), density of water (ρ_f), and viscosity of water (μ) are used to calculate the Reynolds number at each tested flow rate for each sample. This is the same Reynolds number definition as used by Fink et al. on earlier studies of flow through microlattices.[25] The Reynolds number length scale is intentionally not chosen as the square root of permeability so as to enable angular dependence of the flow to be considered independently from the Reynolds number.

$$Re_n = \frac{\rho_f \dot{V} D_n}{A_{flow} \mu \varepsilon_v} \tag{1}$$

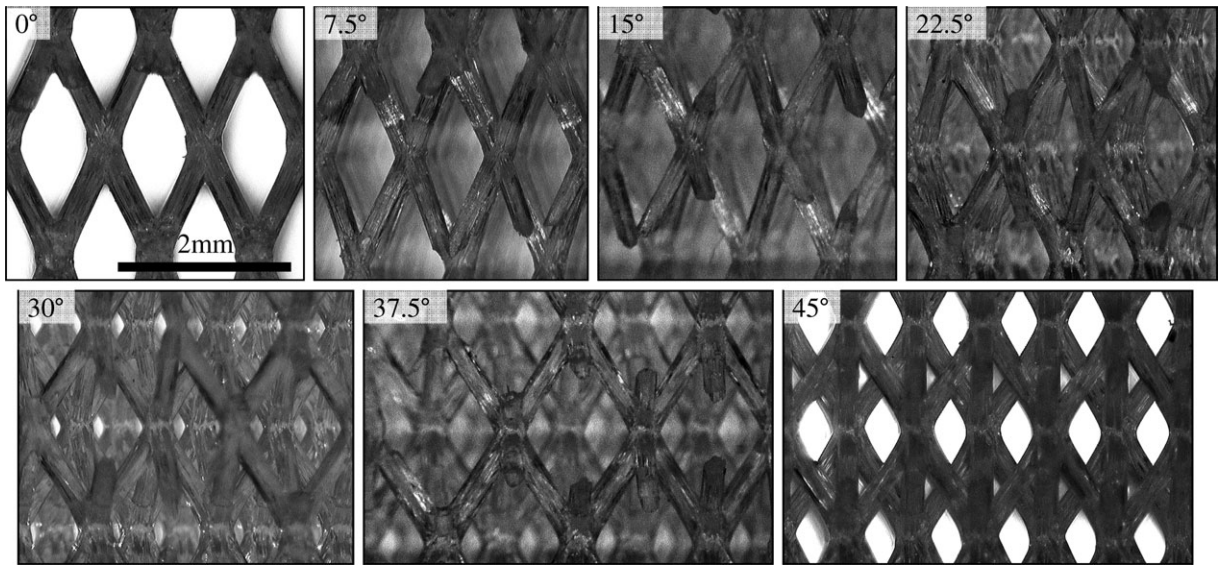

Figure 2. Images of 2.5-cm deep microlattice samples with unit cell spacing L = 1.58 mm and strut aspect ratio L/D = 4.84 cut at varying angles (rear illumination).

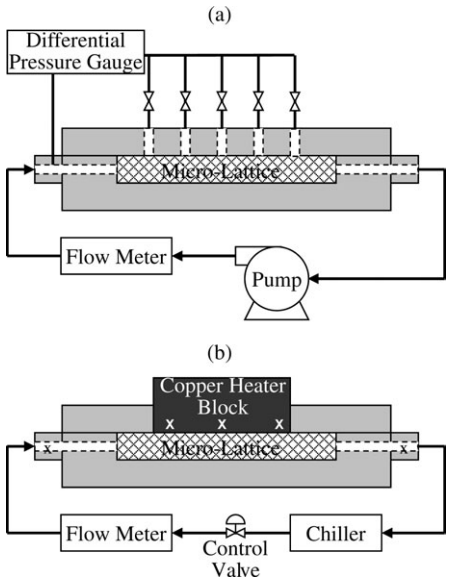

Figure 3. Schematics of measurement setups for (a) fluid flow and (b) heat transfer. "*X*"s denote thermocouple locations.

Linear fits to the measured pressure drop as a function of distance through the sample are used to determine the pressure drop per unit length ($\Delta P/l$) for each sample. From the fluid flow experimental data, the Darcy friction factor (f) is also calculated for each sample and flow condition.

$$f_{\text{Darcy}} = \left(\frac{\Delta P}{l}\right)\frac{2D_{\text{n}}}{\rho_{\text{f}}(\dot{V}/A_{\text{flow}}\varepsilon_{\text{v}})^2} \tag{2}$$

From the heat transfer experimental data, the heat transferred to the water (Q) is calculated from the inlet and outlet temperature of the water (T_{in} and T_{out}), the density of water at the mean water temperature, the heat capacity of the water at the mean water temperature (c_{p}), and the volumetric flow rate of the water. The contribution of viscous dissipation due to flow through a porous medium[27] to the total heat gained by the fluid is calculated to be less than 0.03% for all cases examined in this study; therefore, viscous dissipation is neglected.

$$Q = \dot{V}\rho_{\text{f}}c_{\text{p}}(T_{\text{out}} - T_{\text{in}}) \tag{3}$$

The heat-transfer coefficient (h) is calculated from the heat transferred, the area of the heated copper block adjacent to the chamber (A_{heated}), the mean water temperature ($(T_{\text{out}} + T_{\text{in}})/2$), and the mean of the six temperatures measured at the heated wall (T_{wall}).

$$h = \frac{Q}{A_{\text{heated}}(T_{\text{wall}} - (T_{\text{out}} + T_{\text{in}})/2)} \tag{4}$$

Although the thermal conductivity of the polymer is known (0.27 $\text{Wm}^{-1}\,\text{K}^{-1}$ at 23°C as calculated from density, thermal diffusivity measured by laser flash, ASTM E1461, and heat capacity measured by differential scanning calorimetry, ASTM E1269), the thermal interface resistance between the polymer microlattice nodes and the copper block as well as the extended surface heat transfer fin efficiency equation for this microlattice geometry are unknown. For this reason, the heat-transfer coefficient reported in this work does not separate the contributions from multiple heat transfer pathways. Instead, the heat-transfer coefficient (Eq. 4) includes both convective heat transfer from the copper block directly into the fluid as well as extended surface heat transfer from the copper block, across the copper–polymer thermal interface, conduction through the polymer microlattice, and convection from the polymer into the fluid.

The Nusselt number (Nu_{n}) is calculated from the heat-transfer coefficient, node diameter, and thermal conductivity of water (k).

$$Nu_{\text{n}} = \frac{hD_{\text{n}}}{k} \tag{5}$$

Results and Discussion

The dimensionless fluid flow data are depicted in Figure 4. Friction factor is monotonically decreasing with Reynolds number in all cases and is roughly proportional to the inverse square root of Reynolds number, indicating intermediate flow between the Darcy and Forchheimer regimes.[25,27] The minimum friction factor is realized at a superficial flow orientation of 0 rad. As superficial flow angle increases from 0 to $\pi/8$ rad, the friction factor also increases for any given Reynolds number. For superficial flow orientations of $\pi/8$–$\pi/4$ rad, friction factor is at a maximum, varying little for any given Reynolds number. Error bars in Figure 4 reflect uncertainties in measurements and in sample dimensions. Measurement uncertainty contributes one-third and variation in unit cell parameters contributes two-thirds of the total uncertainty.

Figure 5 depicts the dimensionless heat transfer data where Nusselt number monotonically increases with increasing Reynolds number for each superficial flow orientation. The superficial flow orientation of $\pi/4$ rad yields the highest Nusselt number across most Reynolds numbers; however, there is less spread in the Nusselt numbers than the friction factors. The difference in Reynolds number ranging between Figures 4 and 5 is attributed to extension of the heat transfer tests to lower flow rates and the higher kinematic viscosity of water at the lower temperatures used in the heat transfer study. The Nusselt number expected in the case of fully developed flow in an empty rectangular duct of the same dimensions as the test chamber with constant flux heating

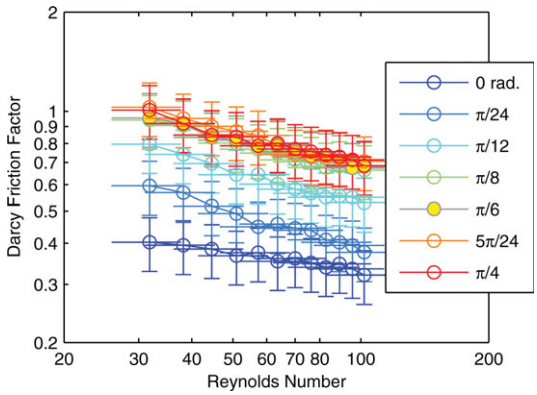

Figure 4. Darcy friction factor versus Reynolds number for flow through microlattice architecture for seven superficial flow angles.

[Color figure can be viewed in the online issue, which is available at wileyonlinelibrary.com.]

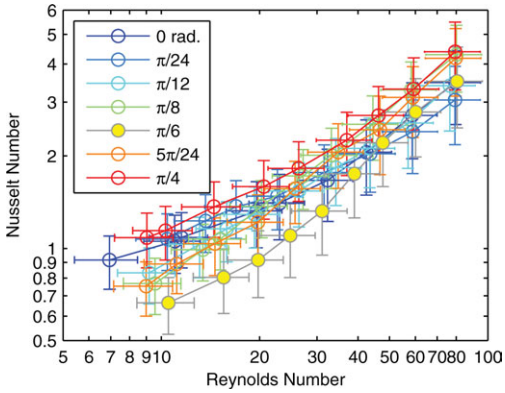

Figure 5. Dimensionless heat transfer data for flow through microlattice architecture for seven superficial flow angles.

[Color figure can be viewed in the online issue, which is available at wileyonlinelibrary.com.]

from one wall is 0.07,[28] significantly lower than the Nusselt numbers found in this study. (N.B. the same length scale, D_n, is used for both the empty channel Nusselt number and the microlattice filled channel Nusselt number to facilitate comparison. The typical length scale choice for empty channel flow, the empty channel hydraulic diameter, would prevent comparison with the microlattice Nusselt number based on microlattice node diameter.) This indicates that the presence of the microlattice confers significant heat transfer enhancement over fully developed flow in an empty channel, as expected. Error bars in Figure 5 reflect uncertainties in measurements and in sample dimensions. Measurement uncertainty contributes half and variation in unit cell parameters contributes half of the total uncertainty.

The relationship between pressure drop and flow rate in porous materials can be described by a sum of the Darcy and non-Darcy flow terms,[29] where K is the permeability and c_f is the Forchheimer inertial coefficient.[30]

$$\frac{\Delta P}{L} = \frac{\mu \dot{V}}{K A_{\text{flow}}} + \frac{\rho c_f \dot{V}^2}{A_{\text{flow}}^2 \sqrt{K}} \tag{6}$$

Nondimensionalizing Eq. 6 yields the following, a simplified version of the Ergun equation useful for analyzing flow in microlattices[25,31]

$$f_{\text{Darcy}} = \frac{B_1}{\text{Re}_n} + B_2 \tag{7}$$

The permeability and the constant, B_1, in Eq. 7 are related

$$K = \frac{2 D_n^2 \varepsilon_v}{B_1} \tag{8}$$

The constant, B_2, in Eq. 7 is related to the Forchheimer inertial coefficient and the permeability

$$c_f = \frac{B_2 \sqrt{K}}{2 D_n \varepsilon_v^2} \tag{9}$$

For isotropic porous media, K and c_f, and thus B_1 and B_2, are independent of flow angle and form circles or spheres when plotted in polar or spherical coordinates, respectively. Anisotropic porous media have constants that vary with flow angle. For previously reported anisotropic porous media, permeabilities form ellipses or rotated ellipses when plotted in polar coordinates,[29] meaning B_1 would be expected to form a hippopede.

Figure 6 plots the nonlinear fitting parameters B_1 and B_2 as a function of flow angle on polar coordinates for the microlattice material. The inverses of the friction factor uncertainties are used to weight the nonlinear fit. The data from the seven samples from $0 \leq \varphi_{\text{rad}} \leq \pi/4$ are repeated on the plot for each geometrically equivalent angle given by the D_{4h} group symmetry of the microlattice. The error bars in Figures 6–8 reflect 95% confidence intervals in the fitting parameters. It is clear that ellipses, circles, or hippopedes do not accurately describe this data. One geometric figure that possess the required symmetry is a superellipse.[32,33]

$$1 = \left|\frac{x}{a}\right|^{2/r} + \left|\frac{y}{b}\right|^{2/r} \tag{10}$$

In Eq. 10, a and b are half of the major axis of the superellipse and half of the minor axis of the superellipse, respectively. Cartesian coordinates are denoted by x and y, whereas r is a parameter that governs the curvature of the superellipse. When $r = 3$, the superellipse is termed an astroid.[33] The angular dependence of the constants in Eq. 7 is fit well by the subtraction of an astroid from a circle. The astroid is oriented with the larger, diamond-shaped through channels (0 rad).

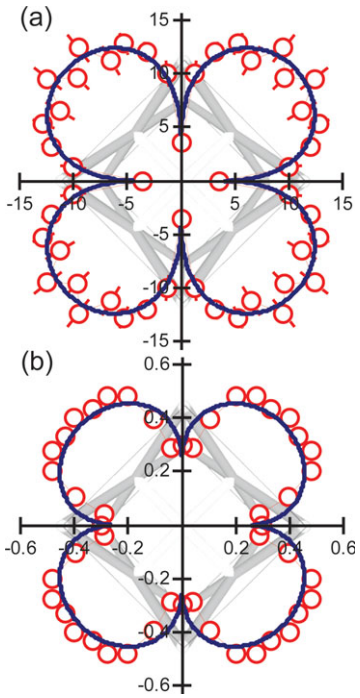

Figure 6. Fluid flow fitting parameters in a microlattice architecture as a function of superficial flow angle.

Red circles connected by thin lines are dimensionless correlation fitting parameters, B_1 (a) and B_2 (b). Thick solid lines are second-level fits to the first-level fitting parameters. Microlattice unit cell geometry is shown in the background. [Color figure can be viewed in the online issue, which is available at wileyonlinelibrary.com.]

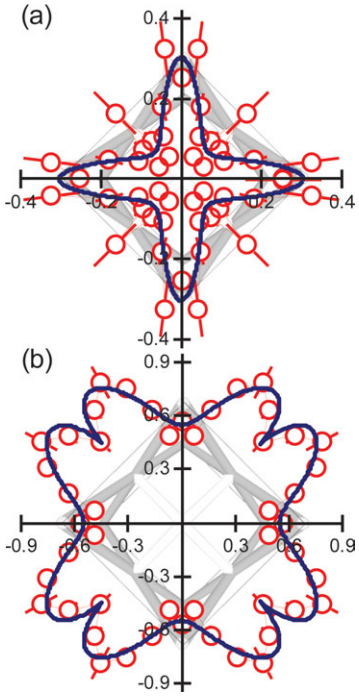

Figure 7. Heat transfer fitting parameters in a microlattice architecture as a function of superficial flow angle.

Red circles connected by thin lines are dimensionless correlation fitting parameters, *C* (a) and *m* (b). Thick solid lines are second-level fits to the first-level fitting parameters. Microlattice unit cell geometry is shown in the background. [Color figure can be viewed in the online issue, which is available at wileyonlinelibrary.com.]

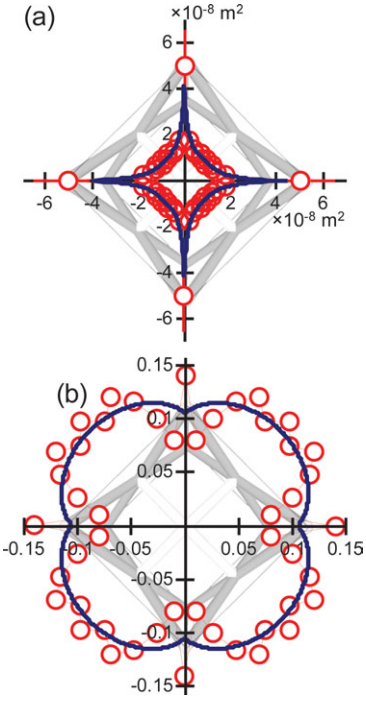

Figure 8. Permeability (a) and Forchheimer inertial coefficient (b) as a function of superficial flow angle.

Microlattice unit cell geometry is shown in the background. [Color figure can be viewed in the online issue, which is available at wileyonlinelibrary.com.]

$$B_1(\phi) = X_2 - X_1\sqrt{\frac{1}{|\cos\ \varphi|^{2/3} + |\sin\ \varphi|^{2/3}}} \tag{11}$$

$$B_2(\phi) = X_2 - X_1\sqrt{\frac{1}{|\cos\ \varphi|^{2/3} + |\sin\ \varphi|^{2/3}}} \tag{12}$$

X_1 and X_2 are fitting parameters. A second level of nonlinear fitting using Eqs. 11 and 12 to the first-level fitting parameters B_1 and B_2 is plotted in Figure 6 and the fitting parameters are tabulated in Table 1. The inverses of the 95% confidence interval ranges for B_1 and B_2 are used to weight the nonlinear fits. The incorporation of astroids accounts well for the difference between the microlattice and random foams. This difference is attributed to the presence of straight-through channels that are present in the microlattice but are not present in random foams.

The Nusselt number–Reynolds number relationship for this microlattice architecture can be expressed as a power law function where C and m are fitting parameters that depend on superficial flow orientation.

$$Nu_n = C(Re_n)^m \tag{13}$$

The results of nonlinear least-squares fits for each of the seven superficial flow orientations are presented in Figure 7. The inverses of the Nusselt number uncertainties are used to weight the nonlinear fits. The seven samples from $0 \leq \varphi_{rad} \leq \pi/4$ are repeated on the plot for each geometrically equivalent angle given by the D_{4h} group symmetry of the microlattice.

The pre-exponential constant, C, ranges from 0.06 to 0.33, while the exponent, m, varies from 0.50 to 0.91. For plate fin geometries, typical pre-exponential constants include 0.2–1.1 and typical exponents include 0.3–0.7.[34] Although the exponent ranges between the polymer microlattice presented in this work and plate fin geometries overlap significantly, the pre-exponential constant for the polymer microlattice only overlaps the very bottom of the range for plate fin geometries. This is expected due to the much lower thermal conductivity of the polymer comprising the polymer microlattice compared to the copper and aluminum plate fin geometries reported by Kays and London.[34] For impinging jets, heat sinks made of aluminum random open-cellular foams, pre-exponential constants range from 9.04×10^{-4} to 2.58×10^{-3} and exponents range from 0.377 to 0.500.[10] Although the exponents are similar between aluminum random open-cellular foams and the polymer microlattice, the pre-exponential constant of aluminum random open-cellular foams is much lower than either the polymer microlattice or typical plate fin geometries.

Table 1. Fitting Parameters for Angular-Dependent Fluid Flow and Heat Transfer Parameters B_1, B_2, C, and m as defined in Eqs. 7, 11–15[a]

	B_1	B_2	C	m
X_1	53.1 ± 12.4	1.35 ± 0.85	N/A	3.10 ± 2.05
X_2	57.1 ± 10.8	1.61 ± 0.74	0.094 ± 0.056	−3.21 ± 2.68
r_1	3*	3*	N/A	0.62 ± 0.07
r_2	N/A	N/A	0.23 ± 0.16	3*

*Denotes geometric form selected as an asteroid prior to fitting, setting $r = 3$.
[a]The range reported after each value indicates the 95% confidence interval.

As with the fluid dynamics fitting constants B_1 and B_2, the angular dependences of the heat transfer fitting constants C and m are inadequately described by circles or ellipses. Instead, it is found that a superellipse oriented by $\pi/4$ rad from the larger, diamond-shaped through channels can be fit to the constant C and a sum of a superellipse and an astroid offset by $\pi/4$ rad can be fit to the exponent n.

$$C(\phi) = X_2 \sqrt{\frac{1}{\left|\cos\left(\varphi + \frac{\pi}{4}\right)\right|^{2/r_2} + \left|\sin\left(\varphi + \frac{\pi}{4}\right)\right|^{2/r_2}}} \tag{14}$$

$$m(\phi) = X_1 \sqrt{\frac{1}{|\cos\varphi|^{2/r_1} + |\sin\varphi|^{2/r_1}}} + X_2 \sqrt{\frac{1}{\left|\cos\left(\varphi + \frac{\pi}{4}\right)\right|^{2/3} + \left|\sin\left(\varphi + \frac{\pi}{4}\right)\right|^{2/3}}} \tag{15}$$

A second level of nonlinear fitting to the first-level fitting parameters C and m is also plotted in Figure 7 and the fitting parameters are tabulated in Table 1. The inverses of the 95% confidence interval ranges for C and m are used to weight the second-level nonlinear fits. Additional superellipses could be added to the correlation functions to increase fit quality, but this would require higher angular resolution because the second-level fit in Figure 7b already uses three parameters to fit only seven points.

Figure 8 replots the data in Figure 6, using Eqs. 8 and 9 to transform the fluid flow fitting parameters B_1 and B_2 into permeability and Forchheimer inertial coefficient. The fits based on Eqs. 11 and 12 are also transformed. Permeability ranges from 1.2×10^{-8} to 5.0×10^{-8} m^2, with the highest permeability occurring for flow aligned with the 0 rad orientation. As expected, this is a significantly higher permeability than most porous media, including sandstone (5×10^{-16}–3×10^{-12} m^2), hot-compacted copper powder (3.3×10^{-10}–1.5×10^{-9} m^2), and sand (2×10^{-11}–1.8×10^{-10} m^2).[27] It is also higher permeability than for flow through aluminum random open-cellular foams (1.75×10^{-10}–1.14×10^{-9} m^2).[15] The Forchheimer inertial coefficient exhibits less variation with angle than permeability. The inertial coefficient varies between 0.08 and 0.14, which is roughly a factor of two lower than the range predicted when applying the equations of Ergun[27,31] in to this microlattice, 0.14–0.29. The inertial coefficient is also lower than for flow through aluminum random open-cellular foams (0.371–0.838).[15]

The ratio of the Colburn j-factor for heat transfer to the Fanning friction factor can be used to understand the efficiency of a geometry for heat sink, cold plate, and heat exchanger applications.[34] This term is a dimensionless ratio of heat transfer to the pressure drop. The Colburn j-factor for heat transfer is defined as[35]

$$j_H = \frac{Nu_n}{Re_n Pr^{1/3}} \tag{16}$$

The Fanning friction factor is one quarter the Darcy friction factor.

$$f_{Fanning} = \frac{f_{Darcy}}{4} \tag{17}$$

Figure 9 depicts the ratio of the Colburn j-factor for heat transfer to the Fanning friction factor for seven superficial flow orientations. The Nusselt number was linearly interpolated between points on Figure 5 to yield values that matched the Reynolds numbers in Figure 4. From Figure 9, it is observed that the optimal orientation for heat transfer with low-pressure head is at 0 rad, corresponding to alignment of the largest straight-through passages with the flow orientation. This agrees with the earlier observation that superficial flow orientation has little effect on heat transfer and that 0 rad orientation yields the lowest pressure drop. A deviation of $\pi/24$ rad from this optimal orientation reduces the efficiency by a factor of 1.4. The least optimal orientation, a deviation of $\pi/6$ rad from the optimal orientation, reduces the efficiency by a factor of 2–2.9 depending on Reynolds number. Moreover, a deviation of $\pi/12$ rad from the optimal flow orientation yields efficiency similar to that for a flow orientation of $\pi/4$ rad. Note that a flow orientation of $\pi/4$ rad corresponds to alignment of the second largest straight-through passages with the flow orientation. Error bars in Figure 9 reflect uncertainties in measurements and in sample dimensions.

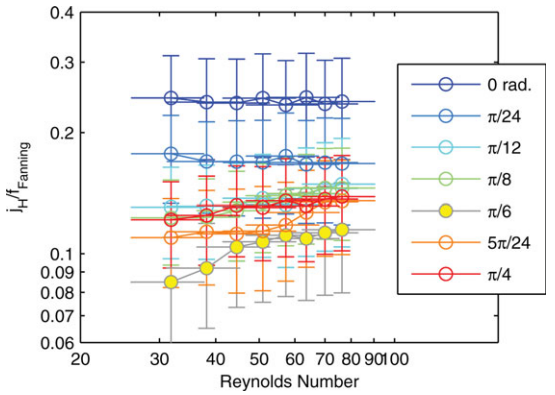

Figure 9. Ratio of Colburn j-factor for heat transfer to Fanning friction factor as a function of Reynolds number for seven superficial flow orientations through a microlattice material.

[Color figure can be viewed in the online issue, which is available at wileyonlinelibrary.com.]

In cases of no form drag, the ratio of the Colburn j-factor for heat transfer to the Fanning friction factor should be 0.5.[36] The ratios in Figure 9 are all below 0.5, indicating form drag is a significant contribution to the friction factor. This is expected for flow around cylindrical bodies, as occurs in this microlattice. Ratios of the Colburn j-factor to the Fanning friction factor with values between 0.2 and 0.4 have been reported for plain plate fin, louvered fin, strip fin, pin fin, wavy fin, and perforated fin heat sink and cold plate geometries[34] at higher Reynolds numbers (500–2000) than those studied in this work. Additionally, Kays and London[34] study highly thermally conductive materials that take better advantage of the extended surface heat transfer enhancement than the thermally insulating polymer microlattices studied in this work. Despite the differences in Reynolds number and materials, the polymer microlattice has heat transfer efficiency on par with some traditional metallic heat sink and cold plate geometries.

Conclusions

The anisotropic fluid dynamics and heat transfer properties of convective flow through a microlattice structure have

been characterized. Friction factor is found to be strongly orientation dependent, while heat transfer is found to be weakly orientation dependent. Angular-dependent correlations to the fluid flow and heat transfer data taking the form of sums and differences of superellipses are found, unlike correlations for random porous media that take the form of circles or ellipses. The optimal orientation for high heat transfer rate with simultaneously low-pressure is to align the superficial flow orientation with the largest straight-through passages in the microlattice material.

It is expected that similar results will be found in three dimensions (3-D). Namely, similar fitting equations are expected to apply in the x–z and y–z planes and the optimal orientation for efficient heat transfer is expected to be aligned with the largest straight-through passages. However, the angular fitting equations would likely involve sums and differences of superellipses with nonequal major and minor axes. Full 3-D angular-dependent correlations for microlattice materials might take the form of sums and differences of superellipsoids.[33] It is also expected that similar results will be found for microlattices with other group symmetries. For instance, microlattices with D_{6h} or D_{3h} group symmetry[23] might fit well with sums and differences of geometric figures described by the superformula given by Gielis[37] with the requisite group symmetry.

The correlations relating friction factor and Nusselt number to superficial flow angle and Reynolds number provide a basis for analytical or numerical optimization of architected materials.[38] Additionally, this work enables design of lightweight, multifunctional microlattice materials[39] with optimal orientation for maximum heat transfer and minimum pressure loss.

Acknowledgments

The authors gratefully acknowledge Robyn Strumpf for setting up the heat transfer measurement system and William Carter for useful discussions.

Notation

a = half of the major axis of an ellipse
A = area, m^2
b = half of the minor axis of an ellipse
B = fluid flow fitting parameter
C = heat transfer fitting parameter
c_f = Forchheimer inertial coefficient, $m^2\ s^2/kg$
c_p = heat capacity, J/(kg K)
D = lattice member diameter, m
f = friction factor
H = heat-transfer coefficient, $W/(m^2\ K)$
j_H = Colburn j-factor for heat transfer
k = thermal conductivity, W/(m K)
K = permeability, m^2
L = unit cell dimension, m
m = heat transfer fitting parameter (exponent)
Nu = Nusselt number
Pr = Prandtl number
Q = heat flow, W
r = second-level fitting parameter
Re = Reynolds number
T = temperature, K
$\dot{V}$ = volumetric flow rate, m^3/s
x = ellipse major axis coordinate
X = second-level fitting parameter
y = ellipse minor axis coordinate
ΔP = pressure drop, Pa
ε_v = porosity
μ = dynamic viscosity, kg/(m s)
ρ = density
φ = superficial flow angle, rad

Subscripts

1 = first parameter
2 = second parameter
Darcy = Darcy definition
Fanning = Fanning definition
flow = cross-sectional to flow direction
heated = heated surface
in = flow inlet
n = node
out = flow outlet
unit cell = pertaining to one unit cell
wall = wall

Literature Cited

1. Kraus AD, Aziz A, Welty J. *Extended Surface Heat Transfer*. New York: Wiley, 2001.
2. Chu RC, Simons RE, Ellsworth MJ, Schmidt RR, Cozzolino V. Review of cooling technologies for computer products. *IEEE Trans Device Mater Reliab*. 2004;4:568–585.
3. Incropera FP, DeWitt DP, Bergman TL, Lavine AS. *Fundamentals of Heat and Mass Transfer*. Wiley, 2007.
4. Jiang P-X, Li M, Lu T-J, Yu L, Ren Z-P. Experimental research on convection heat transfer in sintered porous plate channels. *Int J Heat Mass Transfer* 2004;47:2085–2096.
5. Seo Young Kim J-MK, Kuznetsov AV. Effect of anisotropy in permeability and effective thermal conductivity on thermal performance of an aluminum foam heat sink. *Numer Heat Transfer Part A: Appl*. 2001;40:21–36.
6. Kim SY, Kuznetsov AV. Optimization of pin-fin heat sinks using anisotropic local thermal nonequilibrium porous model in a jet impinging channel. *Numer Heat Transfer Part A: Appl*. 2003; 44:771–787.
7. Kuznetsov AV, Nield DA. The Cheng–Minkowycz problem for cellular porous materials: effect of temperature-dependent conductivity arising from radiative transfer. *Int J Heat Mass Transfer* 2010;53:2676–2679.
8. Nield DA, Kuznetsov AV. The onset of convection in a layer of cellular porous material: effect of temperature-dependent conductivity arising from radiative transfer. *J Heat Transfer* 2010;132: 074503.
9. Nield DA, Kuznetsov AV. Forced convection in cellular porous materials: effect of temperature-dependent conductivity arising from radiative transfer. *Int J Heat Mass Transfer* 2010;53:2680–2684.
10. Shih WH, Chiu WC, Hsieh WH. Height effect on heat-transfer characteristics of aluminum-foam heat sinks. *J Heat Transfer* 2006;128:530–537.
11. Shih WH, Chou FC, Hsieh WH. Experimental investigation of the heat transfer characteristics of aluminum-foam heat sinks with restricted flow outlet. *J Heat Transfer* 2007;129:1554–1563.
12. Lu TJ, Stone HA, Ashby MF. Heat transfer in open-cell metal foams. *Acta Mater*. 1998;46:3619–3635.
13. Ozmat B. Reticulated metal foams build better heatsinks. *Power Electron Technol*. 2007; 24–29.
14. Lage JL, Narasimhan A, Porneala DC, Price DC. In: *Emerging Technologies and Techniques in Porous Media*. Ingham DB, Bejan A, Mamut E, Pop I, editors, Vol. 134. Experimental Study Of Forced Convection Through Microporous Enhanced Heat Sinks, Netherlands: Springer, 2004:433–452.
15. Antohe BV, Lage JL, Price DC, Weber RM. Experimental determination of permeability and inertia coefficients of mechanically compressed aluminum porous matrices. *J Fluids Eng*. 1997;119:404–412.
16. Mahjoob S, Vafai K. A synthesis of fluid and thermal transport models for metal foam heat exchangers. *Int J Heat Mass Transfer* 2008;51:3701–3711.
17. Lu TJ, Valdevit L, Evans AG. Active cooling by metallic sandwich structures with periodic cores. *Prog Mater Sci*. 2005;50:789.
18. Tien CL, Hunt ML. Boundary-layer flow and heat transfer in porous beds. *Chem Eng Process*. 1987;21:53–63.
19. Hunt ML, Tien CL. Effects of thermal dispersion on forced convection in fibrous media. *Int J Heat Mass Transfer* 1988;31:301–309.
20. Jacobsen AJ, Barvosa-Carter W, Nutt S. Micro-scale truss structures formed from self-propagating photopolymer waveguides. *Adv Mater*. 2007;19:3892–3896.
21. Jacobsen AJ, Barvosa-Carter W, Nutt S. Compression behavior of micro-scale truss structures formed from self-propagating polymer waveguides. *Acta Mater*. 2007;55:6724–6733.

22. Jacobsen AJ, Barvosa-Carter W, Nutt S. Shear behavior of polymer micro-scale truss structures formed from self-propagating polymer waveguides. *Acta Mater*. 2008;56:1209–1218.
23. Jacobsen AJ, Barvosa-Carter W, and Nutt S. Micro-scale truss structures with three-fold and six-fold symmetry formed from self-propagating polymer waveguides. *Acta Mater*. 2008;56:2540–2548.
24. Tian J, Kim T, Lu TJ, Hodson HP, Queheillalt DT, Sypeck DJ, Wadley HNG. The effects of topology upon fluid-flow and heat-transfer within cellular copper structures. *Int J Heat Mass Transfer* 2004;47:3171–3186.
25. Fink KD, Kolodziejska JA, Jacobsen AJ, Roper CS. Fluid dynamics of flow through microscale lattice structures formed from self-propagating photopolymer waveguides. *AICHE J*. 2011;57:2636–2646.
26. Vincent A. *Molecular Symmetry of Group Theory*. New York: Wiley, 2001.
27. Nield DA, Bejan A. *Convection in Porous Media.* Springer, USA 1998.
28. Bejan A, Kraus AD. *Heat Transfer Handbook*. Wiley-Interscience: Hoboken, NJ, 2003.
29. Bear J. *Dynamics of Fluids in Porous Media*. New York: Dover Publications, 1988.
30. Whitaker S. The Forchheimer equation: a theoretical development. *Transport Porous Med.* 1996;25:27–61.
31. Ergun S. Fluid flow through packed columns. *Chem Eng Prog*. 1952;48:89–94.
32. Lamé G. *Examen des différentes méthodes employées pour résoudre les problémes de géométrie*. Paris: Mme. Ve. Courcier, 1818.
33. Barr AH. Superquadrics and angle-preserving transformations. *IEEE Comput Graph*. 1981;1:11–23.
34. Kays WM, London AL. *Compact Heat Exchangers*. New York: McGraw-Hill, 1984.
35. Bird RB, Stewart WE, Lightfoot EN. *Transport Phenomena*. New York: Wiley, 2002.
36. Perry RH, Green DW. *Perry's Chemical Engineers' Handbook.* McGraw-Hill, 1997.
37. Gielis J. A generic geometric transformation that unifies a wide range of natural and abstract shapes. *Am J Bot*. 2003;90:333–338.
38. Roper CS. Multiobjective optimization for design of multifunctional sandwich panel heat pipes with micro-architected truss cores. *Int J Heat Fluid Flow* 2011;32:239–248.
39. Maloney KJ, Fink KD, Schaedler TA, Kolodziejska JA, Jacobsen AJ, Roper CS. Multifunctional heat exchangers derived from three-dimensional micro-lattice structures. *Int J Heat Mass Transfer* 2012;55:2486–2493.

Manuscript received Oct. 10, 2011, and revision received Mar. 16, 2012.